Continuation and stability of convective modulated rotating waves in spherical shells

F. Garcia, M. Net, and J. Sánchez

Departament de Física Aplicada, Universitat Politècnica de Catalunya, Campus Nord, Mòdul B4, Jordi Girona Salgado 1–3, 08034 Barcelona, Spain

(Received 22 October 2015; published 15 January 2016)

Modulated rotating waves (MRW), bifurcated from the thermal-Rossby waves that arise at the onset of convection of a fluid contained in a rotating spherical shell, and their stability, are studied. For this purpose, Newton-Krylov continuation techniques are applied. Nonslip boundary conditions, an Ekman number $E = 10^{-4}$, and a low Prandtl number fluid $\mathrm{Pr} = 0.1$ in a moderately thick shell of radius ratio $\eta = 0.35$, differentially heated, are considered. The MRW are obtained as periodic orbits by rewriting the equations of motion in the rotating frame of reference where the rotating waves become steady states. Newton-Krylov continuation allows us to obtain unstable MRW that cannot be found by using only time integrations, and identify regions of multistability. For instance, unstable MRW without any azimuthal symmetry have been computed. It is shown how they become stable in a small Rayleigh-number interval, in which two branches of traveling waves are also stable. The study of the stability of the MRW helps to locate and classify the large sequence of bifurcations, which takes place in the range analyzed. In particular, tertiary Hopf bifurcations giving rise to three-frequency stable solutions are accurately determined.

DOI: 10.1103/PhysRevE.93.013119

I. INTRODUCTION

The study of thermal convection in rotating spherical geometries is important for understanding the dynamics of astrophysical and geophysical phenomena such as the transport of energy in the interior of planets and stars or the differential rotation observed in the atmospheres of the major planets. In addition, magnetic fields of cosmic bodies are generated by convection of electrically conducting fluids in their interiors. In recent decades, many experimental, theoretical, and numerical studies (see, for instance, Refs. [1–6]) devoted to improving the understanding of the basic mechanisms that govern the convection and dynamo action in spherical geometry have appeared. Good reviews can be found in the literature; see, for instance, Refs. [7] and [8].

Most of the setups of laboratory experiments are not well suited for measurements of flows near the onset of convection at small Ekman number, E, and Prandtl number, Pr, so it is difficult to find a description of periodic flows, observed experimentally, in this range of parameters. From the analytical point of view the nonlinear nature of the equations and the spherical geometry of the domain lead to mathematical issues of very difficult treatment. For this reason, the development and improvement of the numerical techniques is basic to go deeply into the study of weakly supercritical nonlinear flows.

In problems having SO(2) symmetry, convection takes the form of waves traveling in the azimuthal direction (thermal Rossby waves for $\mathrm{Pr} = 0.1$), i.e., of rotating waves (RW), when the axisymmetry of the basic conduction state is broken. A secondary Hopf bifurcation gives rise to MRW, which may have different types of spatiotemporal symmetries [9,10]. In Ref. [10] several examples in which rotating waves can exist, such as the Taylor-Couette system or the meandering spiral waves in the Belousov-Zhabotinsky reaction, among others, are described. In the case of rotating spheres, RW and MRW were studied mainly with the help of direct numerical simulations (see Refs. [11–16], among many others). When the azimuthal symmetry of the equations is constrained, time integrations allow us to obtain some unstable MRW and their bifurcation diagrams [17]. However, the only use of time integrations is not sufficient to provide a complete picture of the dynamics. Specifically, time integration methods are unable to obtain unstable oscillatory solutions when all the symmetries of the flow are broken. These solutions might be relevant in organizing the global dynamics [18]. To find them and provide a deeper description of the phase space, continuation methods [19–22] must be used.

In the fluid dynamics context numerical bifurcation analysis has been successfully applied in recent years to a great variety of problems [18,23–26]. Computations based on continuation of periodic orbits of nontrivial time dependence [27] and even tori [28,29] or other invariant objects [30] have provided useful information to clarify the dynamics. In the case of rotating spherical geometries the bifurcation diagrams and the stability of the RW in the slowly rotating regime, for $\mathrm{Pr} = 1$, were studied in Ref. [31] with nonslip boundary conditions by means of Newton's method. At lower E and Pr, and for a radius ratio $\eta = 0.35$ corresponding to the estimated Earth's outer core, Newton-Krylov continuation techniques and Arnoldi methods were applied successfully in Ref. [32] to explain the coexistence of stable RW due to the presence of a double-Hopf bifurcation, and to understand the existence of amplitude and shape MRW from the symmetry breaking of the eigenfunctions at the secondary bifurcations.

Aside from the use of nonslip boundary conditions and low $\mathrm{Pr} = 0.1$ and $E = 10^{-4}$ values, the main novelty of this study is to obtain branches of MRW bifurcated from the RW previously studied in Ref. [32], using continuation techniques and to perform a stability analysis of these waves to study bifurcations to more complex flows such as three-frequency waves. The MRW are obtained as periodic orbits by rewriting the equations of motion in the rotating frame of reference in which the RW are steady solutions.

The paper is organized as follows. In Sec. II we introduce the formulation of the problem and briefly describe the numerical method used to obtain and integrate the discretized equations. In Sec. III preceding results concerning the calculation of the RW are summarized. In Sec. IV the equations for

the MRW and the continuation and stability analysis methods are explained. The bifurcation diagrams as a function of the Rayleigh number, Ra, and the patterns of convection are shown in Sec. V, focusing mainly on the results that cannot be studied with just time integrations. Finally, in Sec. VI the paper ends with a brief summary of the results obtained.

II. THE MODEL AND THE EQUATIONS

We consider the thermal convection of a fluid filling the gap between two concentric spheres differentially heated, rotating about an axis of symmetry with constant angular velocity $\Omega = \Omega\mathbf{k}$, and subject to radial gravity $\mathbf{g} = -\gamma\mathbf{r}$, where γ is constant and $\mathbf{r}$ the position vector. The mass, momentum, and energy equations are written in the rotating frame of reference. The units are $d = r_o - r_i$ for the distance, $\nu^2/\gamma\alpha d^4$ for the temperature, and d^2/ν for the time. In the previous definitions r_i and r_o are the inner and outer radii, respectively, ν the kinematic viscosity, and α the thermal expansion coefficient.

We use the Boussinesq approximation, and the solenoidal velocity field is expressed in terms of toroidal, Ψ, and poloidal, Φ, potentials:

$$\mathbf{v} = \nabla \times (\Psi\mathbf{r}) + \nabla \times \nabla \times (\Phi\mathbf{r}). \tag{1}$$

Consequently, the equations for both potentials, and the temperature perturbation, $\Theta = T - T_c$, from the conduction state $\mathbf{v} = \mathbf{0}$, $T = T_c(r)$, with $r = |\mathbf{r}|$ and $T_c(r) = T_0 + \mathrm{Ra}\,\eta/\mathrm{Pr}(1-\eta)^2 r$, are

$$\left[(\partial_t - \nabla^2)L_2 - 2E^{-1}\,\partial_\varphi\right]\Psi = -2E^{-1}\mathcal{Q}\Phi - \mathbf{r}\cdot\nabla\times(\boldsymbol{\omega}\times\mathbf{v}), \tag{2}$$

$$\left[(\partial_t - \nabla^2)L_2 - 2E^{-1}\,\partial_\varphi\right]\nabla^2\Phi + L_2\Theta = 2E^{-1}\mathcal{Q}\Psi + \mathbf{r}\cdot\nabla\times\nabla\times(\boldsymbol{\omega}\times\mathbf{v}), \tag{3}$$

$$\left(\mathrm{Pr}\partial_t - \nabla^2\right)\Theta - \mathrm{Ra}\,\eta\,(1-\eta)^{-2}r^{-3}L_2\Phi = -\mathrm{Pr}(\mathbf{v}\cdot\nabla)\Theta, \tag{4}$$

where $\boldsymbol{\omega} = \nabla \times \mathbf{v}$ is the vorticity.

The parameters of the problem are the Rayleigh number Ra, the Prandtl number Pr, the Ekman number E, and the radius ratio η. They are defined by

$$\mathrm{Ra} = \frac{\gamma\alpha\Delta T d^4}{\kappa\nu}, \quad E = \frac{\nu}{\Omega d^2}, \quad \mathrm{Pr} = \frac{\nu}{\kappa}, \quad \eta = \frac{r_i}{r_o}, \tag{5}$$

where κ is the thermal diffusivity, and $\Delta T > 0$ the difference in temperature between the inner and outer boundaries.

The operators L_2 and $\mathcal{Q}$ are defined by $L_2 \equiv -r^2\nabla^2 + \partial_r(r^2\partial_r)$, $\mathcal{Q} \equiv r\cos\theta\nabla^2 - (L_2 + r\partial_r)(\cos\theta\partial_r - r^{-1}\sin\theta\partial_\theta)$, (r,θ,φ) being the spherical coordinates, with θ measuring the colatitude, and φ the longitude. Nonslip perfect thermally conducting boundaries are used:

$$\Phi = \partial_r\Phi = \Psi = \Theta = 0 \quad \text{at} \quad r = r_i, r_o. \tag{6}$$

The equations are discretized and integrated as described in Ref. [33] and references therein. The potentials and the temperature perturbation are expanded in spherical harmonics in the angular coordinates, truncated at degree $L_{\max}$. In the radial direction a collocation method on a Gauss-Lobatto mesh of $n_r + 1$ points is used. The code is parallelized in the spectral and physical spaces by using OpenMP directives (see Ref. [34]). We use optimized libraries (FFTW3 [35]) for the FFTs in φ and matrix-matrix products (DGEMM GOTO [36]) for the Legendre transforms in θ when computing the nonlinear terms.

For the time integration high-order implicit-explicit backward differentiation formulas (IMEX–BDF) [33] are used. In the IMEX method we treat the nonlinear terms explicitly in order to avoid solving nonlinear equations at each time step. The Coriolis term is treated fully implicitly to allow larger time steps. The use of matrix-free Krylov methods (GMRES in our case) for the linear systems facilitates the implementation of a suitable order and time step-size control.

III. COMPUTATION AND STABILITY OF THE ROTATING WAVES

In this section some background necessary to follow easily Secs. IV and V is included.

The discretization of Eqs. (2)–(4) leads to a system of $n = (3L_{\max}^2 + 6L_{\max} + 1)(n_r - 1)$ ordinary differential equations (ODE) of the form

$$L_0\partial_t u = Lu + B(u,u), \tag{7}$$

where $u = (\Psi_l^m(r_i), \Phi_l^m(r_i), \Theta_l^m(r_i))$ is the vector containing the values of the spherical harmonic coefficients at the inner radial collocation points, and L_0 and L are linear operators which include the boundary conditions. The former is invertible. It is the identity acting on Ψ_l^m and Θ_l^m, and the operator $\mathcal{D}_l$ acting on Φ_l^m (see Ref. [32] for details). The operator L includes all the linear terms and depends on the parameters of the problem, in particular on the Rayleigh number Ra, which will be the control parameter of this study. The rest of parameters are fixed to $\eta = 0.35$, $E = 10^{-4}$, and $\mathrm{Pr} = 0.1$. Therefore, $p = \mathrm{Ra}$ and $L = L(p)$. The bilinear operator B only contains the nonlinear (quadratic) terms.

The system is $\mathrm{SO}(2) \times \mathcal{Z}_2$-equivariant, $\mathrm{SO}(2)$ generated by azimuthal rotations, and $\mathcal{Z}_2$ by reflections with respect to the equatorial plane. According to bifurcation theory, the first bifurcation, which breaks the axisymmetry of the conductive state, is a Hopf bifurcation giving rise to RW. In the linear stability analysis of Refs. [37] and [32], critical values $p = p_1$, at which there are vectors v_c and precession frequencies ω_c satisfying $i\omega_c L_0 v_c = Lv_c$, were obtained as a function of E and η, respectively. With $\mathrm{Pr} = 0.1$, $\eta = 0.35$, and $E = 10^{-4}$ the preferred eigenfuctions are symmetric with respect to the equator. The precession frequencies ω_c are negative, namely the drifting velocities $c = -\omega_c/m$ are positive, thus the waves travel in the prograde direction. Moreover, they consist in quasigeostrophic convective columns attached to the inner sphere of mean radius $r_c \ll d$.

Rotating waves, $u(r,\theta,\varphi - \omega t) = \tilde{u}(r,\theta,\tilde{\varphi})$, with $\tilde{\varphi} = \varphi - \omega t$, were obtained in Ref. [32] by Newton-Krylov continuation methods as steady solutions of the system (omitting the tildes),

$$F(u,\omega,p) \equiv L(p)u + B(u,u) + \omega L_0\partial_\varphi u = 0, \tag{8}$$

by using a suitable preconditioner to accelerate the convergence of the linear solver. Their stability was studied by considering a perturbation $v(t,r,\theta,\tilde{\varphi})$ of $u(r,\theta,\tilde{\varphi})$ and

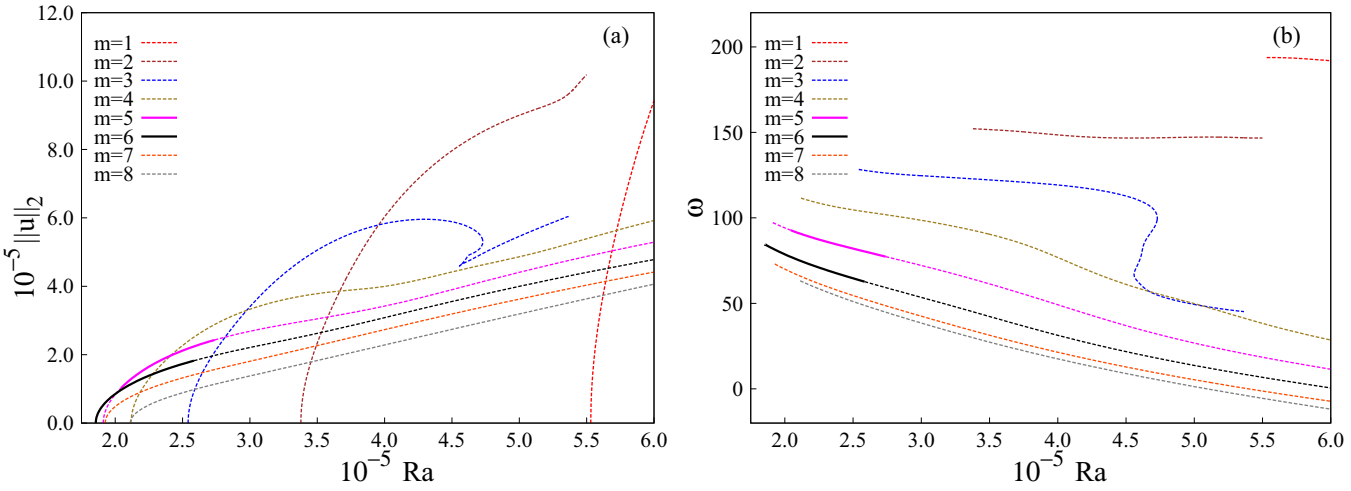

FIG. 1. Bifurcation diagram (taken from Ref. [32]) showing (a) the $\mathcal{L}_2$-norm of the RW and (b) the drifting frequency, ω, both versus Ra. The order of the branches is $m = 6, 5, 7, 8, 4, 3, 2, 1$.

linearizing Eq. (8). The leading eigenvalues of the matrix $L_0^{-1} D_u F(u)$ were computed using the ARPACK package [38], based on Arnoldi algorithms, and shift-invert strategies [39].

The bifurcation diagrams were calculated for the values of the parameters above mentioned, i.e., for $E = 10^{-4}$, $\mathrm{Pr} = 0.1$, control parameter $p = \mathrm{Ra}$, and different values of the radius ratio η, around the vicinity of a double-Hopf bifurcation.

Figures 1(a) and 1(b), taken from Ref. [32], show the $\mathcal{L}_2$-norm of the RW and the drifting frequency, ω, respectively, versus Ra for $\eta = 0.35$. The horizontal axis in Fig. 1(a) corresponds to the basic conductive state $\|u\|_2 = 0$. In these figures, solid and dashed lines indicate stable and unstable solutions, respectively. The preferred mode at the onset of convection ($\mathrm{Ra}_c = 1.856 \times 10^5$), has a sixfold rotational symmetry. At the bifurcation point a branch of supercritical stable RW keeping this symmetry emerges. Other branches bifurcated from the conduction state at higher Ra, invariant under $2\pi/m$ rotations ($m = 5,7,8,4,\cdots$), are unstable. However, that with the fivefold symmetry stabilizes after a Hopf bifurcation at $\mathrm{Ra} = 2.043428 \times 10^5$, which breaks the fivefold symmetry. An unstable branch of MRW without any azimuthal symmetry is born at this point. This behavior was related with the existence of a double-Hopf bifurcation at a slightly different value of η (0.3308), involving the modes of azimuthal wave numbers $m = 5$ and $m = 6$. The branches of five- or sixfold symmetric RW lose their stability via new Hopf bifurcations at $\mathrm{Ra} = 2.584388 \times 10^5$ and $\mathrm{Ra} = 2.738518 \times 10^5$, giving rise to branches of stable MRW, which keep the symmetry of the RW.

IV. COMPUTATION AND STABILITY OF THE MODULATED ROTATING WAVES

As said before, the RW undergo secondary Hopf bifurcations at critical values p, giving rise to branches of MRW. These are solutions for which there exist a minimal time $\tau > 0$ and a rotating frequency ω, such that

$$u(\tau + t, r, \theta, \varphi) = u(t, r, \theta, \varphi - \omega\tau) \quad \forall t. \tag{9}$$

The time τ is the period of the modulation in the frame of reference at which only the oscillations due to the modulation are observed, and ω is the angular velocity of this frame of reference (relative to the rotating spheres).

Let us define $u(t,r,\theta,\varphi) = \tilde{u}(t,r,\theta,\tilde{\varphi})$, with $\tilde{\varphi} = \varphi - \omega t$ and ω a rotating frequency. If $\tilde{u}$ is a τ-periodic function, then u is a MRW because

$$u(t+\tau,r,\theta,\varphi) \overset{1}{=} \tilde{u}(t+\tau,r,\theta,\varphi - \omega(t+\tau)) \overset{2}{=}$$

$$\overset{2}{=} \tilde{u}(t,r,\theta,\varphi - \omega t - \omega\tau) \overset{3}{=} u(t,r,\theta,\varphi - \omega\tau).$$

Identities 1 and 3 are due to the definition of $\tilde{u}$, while equality 2 is because $\tilde{u}$ is a τ periodic function.

Taking into account that $\partial_t u = \partial_t \tilde{u} - \omega \partial_{\tilde{\varphi}} \tilde{u}$ and Eq. (7), the equations for $\tilde{u}(t,r,\theta,\tilde{\varphi})$ are deduced. By omitting the tildes, they are

$$\partial_t u = L_0^{-1}(L(p)u + B(u,u)) + \omega \partial_\varphi u. \tag{10}$$

The periodic orbits of this system are MRW of Eq. (7), and its fixed points correspond to RW of Eq. (7).

A. Continuation of the MRW

To study the dependence of the MRW on the parameter $p = \mathrm{Ra}$, pseudoarclength continuation methods are used. They allow to obtain the curve of solutions $x(s) = (u(s),\tau(s),\omega(s),p(s)) \in \mathbb{R}^{n+3}$, s being the arclength parameter, by adding the pseudoarclength condition,

$$m(u,\tau,\omega,p) \equiv \langle w, x - x^0 \rangle = 0, \tag{11}$$

$x^0 = (u^0,\tau^0,\omega^0,p^0)$ and $w = (w_u, w_\tau, w_\omega, w_p)$ being the predicted point and the tangent to the curve of solutions, respectively, obtained by extrapolation of the previous points along the curve.

The system that determines a single solution, $x = (u,\tau,\omega,p)$, is

$$H(u,\tau,\omega,p) = \begin{pmatrix} u - \phi(\tau,u,\omega,p) \\ g(u) \\ h(u) \\ m(u,\tau,\omega,p) \end{pmatrix} = 0, \tag{12}$$

where $\phi(\tau,u,\omega,p)$ is solution of Eq. (10) at time $t=\tau$ with initial condition u at $t=0$, and for fixed ω and p. The conditions $g(u)=0$ and $h(u)=0$ are selected to fix the two undetermined phases of the MRW. We use $g(u)=\langle u,\partial_\varphi u_c\rangle = 0$ and $h(u)=\langle u,\partial_\varphi^3 u_c\rangle = 0$, where u_c is a reference solution (the eigenvector, $u_c=v_c$, at $p=p_2$, a previously computed solution, or the extrapolated value of u at the first iteration). The former is a necessary condition for $\|u-u_c\|_2^2$ to be minimal with respect to the phase (see Ref. [32]), and the latter is selected to ensure $h(u_c)=0$. For the computation of the inner products $\langle\cdot,\cdot\rangle$ between two functions expanded in spherical harmonics we use the definitions of Ref. [32].

To solve the large nonlinear system defined by Eq. (12) we use Newton-Krylov methods. They are matrix-free methods that do not require the explicit computation of the jacobian $D_{(u,\tau,\omega,p)}H(u,\tau,\omega,p)$, but only its action on a given vector. For the linear systems we use GMRES [40]. Due to the particular form of the spectrum of $D_{(u,\tau,\omega,p)}H(u,\tau,\omega,p)$ for dissipative systems, GMRES does not need preconditioning (see Ref. [20] for details).

The action of the Jacobian $D_{(u,\tau,\omega,p)}H(u,\tau,\omega,p)$ on $\delta x=(\delta u,\delta\tau,\delta\omega,\delta p)\in\mathbb{R}^{n+3}$ is

$$\begin{pmatrix} \delta u - v(\tau) - \dot{z}(\tau)\delta\tau \\ D_u g(u)\delta u \\ D_u h(u)\delta u \\ D_x m(x)\delta x \end{pmatrix} \in \mathbb{R}^{n+3}. \tag{13}$$

Here $z(\tau),v(\tau)\in\mathbb{R}^n$ are the solutions, at time $t=\tau$, of the system

$$\partial_t z = L_0^{-1}(L(p)z + B(z,z)) + \omega\partial_\varphi z, \tag{14}$$

$$\begin{aligned}\partial_t v =& L_0^{-1}(L(p)v + B(z,v) + B(v,z)) \\ &+ \omega\partial_\varphi v + \delta\omega\partial_\varphi z + \delta p L_0^{-1}L^{(2)}z,\end{aligned} \tag{15}$$

with initial conditions $z(0)=u$ and $v(0)=\delta u$, with fixed ω and p. The dependence of L on p, of the form $L(p)=L^{(1)}+pL^{(2)}$ has been used. Each GMRES iteration will require one evaluation of the Jacobian, therefore most of the computational cost is consumed in the integration over one tentative modulation period of a large ODE system of dimension $2n$. Thus, an efficient time integration is mandatory.

Notice that the RW can be obtained with the code written to compute MRW by omitting the term $\omega\partial_\varphi u$ in Eq. (10), and the dependence of ω and the phase condition $h(u)$ of Eq. (12). In this case τ means the period of the RW. However, the time integration can be reduced by a factor m due to their m-fold spatial symmetries. Moreover, since the fixed points of system Eq. (10) are RW of system Eq. (7), they can also be computed with the same code by removing the dependence on τ and one phase condition in Eq. (12). Now the flying time τ appearing in the first component of Eq. (12) is no longer an unknown but a fixed characteristic time. It should be small to avoid long-time integrations but large enough to have a fast convergence of the linear solver. We have used these tricks to check the new code for the computation of MRW by comparing with previous results. These calculations are more demanding than those used in Ref. [32] because they involve time integrations of $2n$ equations, but they are easier to implement, if a time-stepper code is available, because GMRES does not need preconditioning in contrast to what happened in Ref. [32].

B. Stability of the MRW

Suppose a MRW $(u,\tau,\omega,p)\in\mathbb{R}^{n+3}$ has been found. To study the stability of this periodic solution, Floquet theory is applied. Handling the full Jacobian matrix $D_u\phi(\tau,u,\omega,p)$, $\phi(\tau,u,\omega,p)$ being the solution of Eq. (10) at time $t=\tau$ with initial condition u at $t=0$ and for fixed ω and p, would require a prohibitive amount of memory due the high resolutions employed in the present study. It is enough to compute the leading eigenvalues and eigenvectors of the map $\delta u \longrightarrow D_u\phi(\tau,u,\omega,p)\delta u = v(\tau), v(\tau)$ being the solution of the first variational equation obtained by integrating the system,

$$\begin{aligned}\partial_t z &= L_0^{-1}(L(p)z + B(z,z)) + \omega\partial_\varphi z,\\ \partial_t v &= L_0^{-1}(L(p)v + B(z,v) + B(v,z)) + \omega\partial_\varphi v,\end{aligned}$$

of dimension $2n$, with initial conditions $z(0)=u$ and $v(0)=\delta u$, over a modulation period τ, with fixed ω and p.

The leading eigenvalues of the map, which correspond to the leading Floquet multipliers, are computed by using the ARPACK package. MRW with leading Floquet multipliers with modulus larger (smaller) than $+1$ are unstable (stable). Notice that in this problem, for any value of p, there are two marginal $(+1)$ Floquet multipliers due to the invariance under azimuthal rotations and time translations, with associated eigenfunctions $v_1=\partial_t u$ and $v_2=\partial_\varphi u$. To avoid unnecessary computations they can be deflated by computing the eigenvalues of the map $\delta u \longrightarrow v(\tau) - \langle v(\tau),v_1\rangle v_1 - \langle v(\tau),v_2\rangle v_2$. This method to determine the stability of the solutions is very robust but computationally expensive because it requires the time integration of and ODE system of dimension $2n$ over one period of the modulation. Since the solution is a periodic orbit of Eq. (10) there is no cheaper alternative to this procedure.

V. RESULTS

Branches of modulated waves

The eigenfunctions at the bifurcation points of Fig. 1 were used to identify the azimuthal symmetries of the MRW and in this way to build initial conditions to start their continuation. The modulation periods $\tau_i^m = 2\pi/\mathrm{Im}(\lambda_i^m)$ of the branches of MRW at the critical parameters p_i^m are obtained from the leading eigenvalues, λ_i^m, at the Hopf bifurcations. The initial drifting frequencies ω_i^m are those of the RW, (u_i^m,ω_i^m,p_i^m), at the bifurcation points. All the results shown in this section (otherwise mentioned) are obtained with truncation parameters $n_r=32$ and $L_{\max}=60$.

Figure 2(a) and their blowups in Figs. 2(b)–2(d) display the drifting frequency, ω, versus Ra for the RW with five- or sixfold rotational symmetry in red (light gray) and for the MRW without any azimuthal symmetry ($m=1$ MRW from now on) and those with five- or sixfold rotational symmetries in blue (dark gray). The meaning of dashes and symbols can be seen in the figure caption. While for the RW the frequency ω always decreases monotonically, for the five- or sixfold symmetric MRW it increases at the beginning of the branch

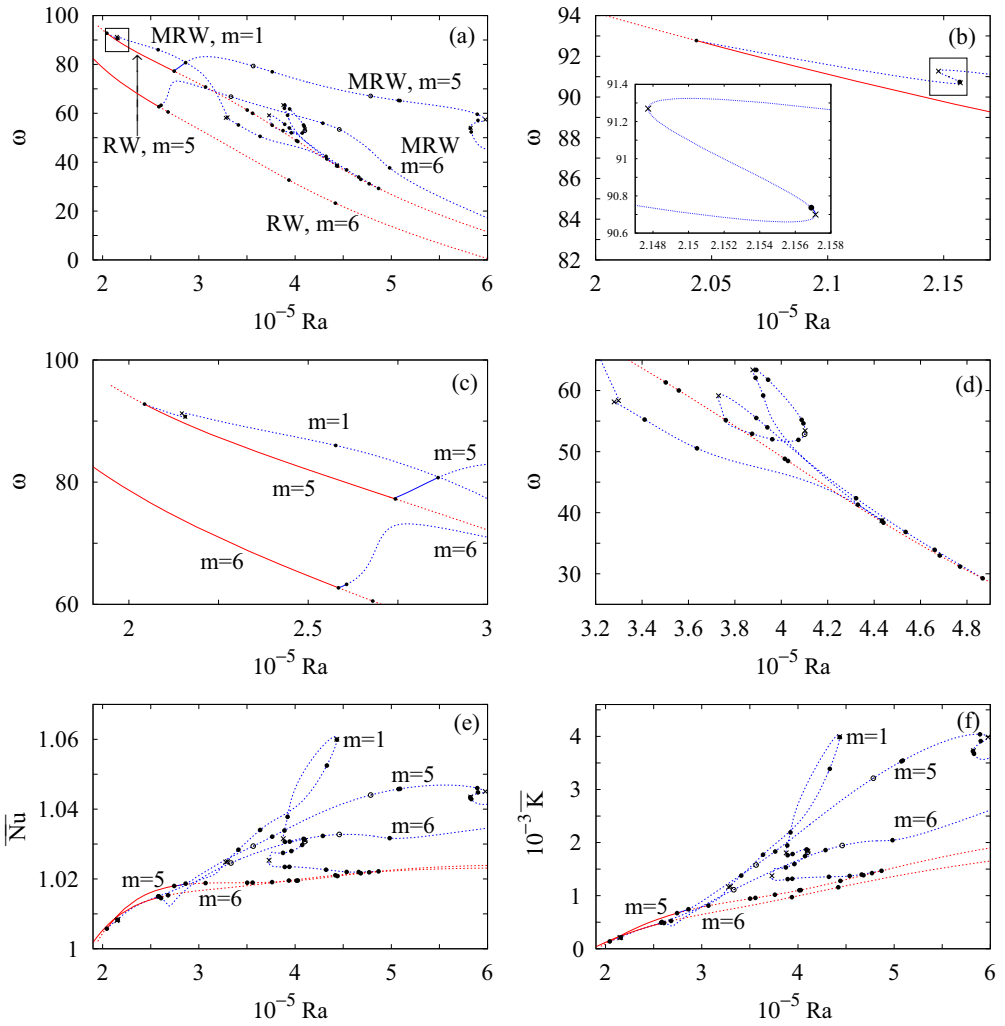

FIG. 2. Bifurcation diagrams: (a) Drifting frequency, ω, versus Ra. (b) Detail corresponding to the square drawn in (a). (c) Detail containing the regions of stable RW and MRW. (d) Detail showing the loops on the $m = 1$ branch of MRW and the fivefold branch of RW. (e) Time-averaged Nusselt number, $\overline{Nu}$, and (f) time-averaged kinetic energy density, $\overline{K}$, both versus Ra. Solid (dashed) lines indicate stable (unstable) solutions. The symbols mean the types of bifurcations: (•) Hopf, (×) saddle-node, and (○) period-doubling.

but starts to decrease soon. In contrast, the behavior of $m = 1$ MRW is more complex. On average, ω decreases, but it increases in the regions where saddle-node bifurcations are present [see Figs. 2(b) and 2(d)].

As said before, the unstable $m = 1$ branch of MRW arises from the fivefold symmetric branch of RW [see Fig. 2(b)]. At a saddle-node bifurcation at $\mathrm{Ra}_1^1 = 2.15713 \times 10^5$ it becomes stable down to $\mathrm{Ra}_2^1 = 2.15690 \times 10^5$, where a Hopf bifurcation occurs. This interval of stability is very small, as shows the detail of Fig. 2(b), so it would be nearly impossible to capture it with direct simulations. The stability analysis of the solutions along this branch has allowed us to identify several bifurcations. The detail of most of the saddle points is shown in Fig. 2(d). Notice that in the latter figure some of the bifurcations are very close, therefore if a second parameter is varied (for instance E or Pr) codimension two bifurcations (Hopf-saddle-node, double-Hopf, period-doubling-saddle-node) could be located. Finally, the branch of $m = 1$ MRW ends at a Hopf bifurcation again on the fivefold symmetric branch of RW [see right-bottom corner of Fig. 2(d)].

In contrast to the $m = 1$ branch of MRW, the regions of stability of the six- and fivefold MRW are sufficiently large [see Fig. 2(c)] as to capture these solutions by time integration [41]. We have identified the bifurcations on these branches and checked that the MRW starting at the first period-doubling bifurcation found correspond to the solutions computed in Ref. [17] by using azimuthal-symmetry-constrained time integration. In the latter work, in agreement with Feigembaum's theory, up to three period-doublings leading to chaotic solutions were found.

The bifurcation diagrams of the time-averaged Nusselt number, $\overline{Nu}$, and kinetic energy density, $\overline{K}$, both defined as in Ref. [42], are shown in Figs. 2(e) and 2(f), respectively. The curves of RW are very smooth and $\overline{Nu}$ and $\overline{K}$ increase monotonically with increasing Ra. In contrast, the curves of MRW are not monotonous and the $m = 1$ branch has a marked loop.

Note that at $\mathrm{Ra} = 4.1 \times 10^5$ there are five unstable solutions without azimuthal symmetries and very different values of $\overline{Nu}$ and $\overline{K}$. The $m = 1$ branch of MRW has the larger $\overline{Nu}$, with

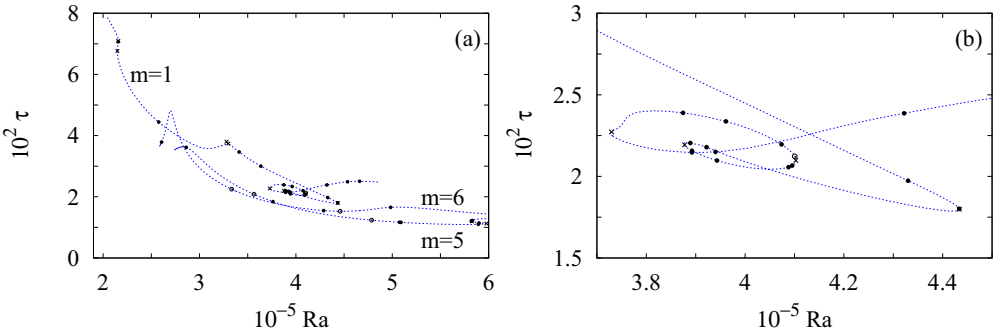

FIG. 3. (a) Bifurcation diagram of the modulation period, τ, of the MRW versus Ra. (b) Detail showing the loop of the $m = 1$ branch. The type of dash and symbols mean the same as described in the caption of Fig. 2

the maximum very near from a Hopf-saddle-node bifurcation (the saddle-node at $\mathrm{Ra}^1_{12} = 4.43366 \times 10^5$ and the Hopf point at $\mathrm{Ra}^1_{11} = 4.43358 \times 10^5$). This solution has also large values of $\overline{K}$ comparable to those of the fivefold symmetric MRW around $\mathrm{Ra} = 5.8 \times 10^5$.

In Fig. 3(a) the modulation period τ for the three branches of MRW shown in Fig. 2 is plotted versus Ra, with a detail in Fig. 3(b) of the double-loop where the $m = 1$ branch undergoes several bifurcations. Each branch of Fig. 3(a) starts with a modulation period τ given by the stability analysis of the RW at the corresponding bifurcation point. It is worth noticing that the theoretically predicted τ could not be minimal in the sense that there might exist another modulation period $\tau' = \tau/k$ with $k \in \mathbb{N}$, and another drifting frequency $\omega' = \omega - 2\pi/\tau$ such that (u, τ', ω', p) is also a MRW (see Ref. [9]). For the five- or sixfold branches the modulation period τ obtained from the stability analysis is minimal. However, for the $m = 1$ MRW the minimal period is $\tau' = \tau/5$. Detecting τ' is important to avoid unnecessary time integrations, which are the most expensive computational task. An algorithm to obtain τ' and ω' directly from an observable of an experiment with $O(2)$ symmetry was presented in Ref. [43]. The modulation period is obtained from the period of the time series of a volume-averaged quantity. This also applies to our problem because volume-averaged quantities are invariant under azimuthal rotations.

Figure 4, showing the modulus of the two leading Floquet multipliers, $|\mu_1| \geqslant |\mu_2|$, plotted versus the Rayleigh number, helps to illustrate how the $m = 1$ branch of MRW gains and loses stability in the doublefold of Fig. 2(b). The modulus of μ_1 is plotted in solid line and $|\mu_2|$ in dashed line. The symbol • signals the values of $|\mu_1|$ and $|\mu_2|$ at the starting point, and the arrows indicate the path followed along the curve. The crossings through the horizontal line placed at $|\mu| = 1$ mark the three bifurcation points along the curve. At the beginning both multipliers are real. When the first crosses the unit circle it stabilizes the fluid at the first saddle-node bifurcation. Afterwards, it collapses with the second forming a complex conjugated pair of $|\mu| < 1$ that crosses again the unit circle. This is the Hopf bifurcation that destabilizes the $m = 1$ branch of MRW. Finally, the pair separates after colliding on the real axis. The first real multiplier increases its modulus and the second crosses again the unit circle at the second saddle-node bifurcation.

Figure 4(b) displays the 20 first leading Floquet multipliers for the last solution computed on the $m = 1$ branch of MRW, which ends again on the fivefold RW. There are nine complex conjugated pairs, eight of them outside the unit circle, and two real, so close to each other, that are indistinguishable in the figure. One of them is outside the unit circle. This means that several of the bifurcations detected along this branch (as much as 29) are due to multipliers entering to the unit circle. Except in the three Hopf bifurcations where the stable MRW lose their stability, any other Hopf or period-doubling bifurcations gives rise to unstable three-frequency solutions or period-doubled MRW, respectively. For instance, 20 branches of unstable objects are born along only the $m = 1$ branch. Thus, the phase space of this problem is so complex that it is almost impossible to unfold a small part of the full bifurcation diagram. However, in some cases, as in Ref. [32], chaotic finite-amplitude solutions at this range of parameters can be

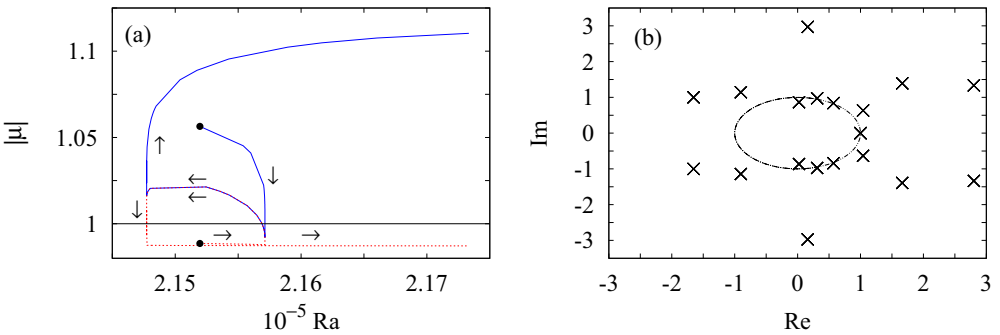

FIG. 4. (a) Modulus of the two leading Floquet multipliers versus Ra, for the solutions shown in the detail of Fig. 2(b). (b) Leading Floquet multipliers of the last solution calculated on the $m = 1$ branch. The closed curve is the unit circle.

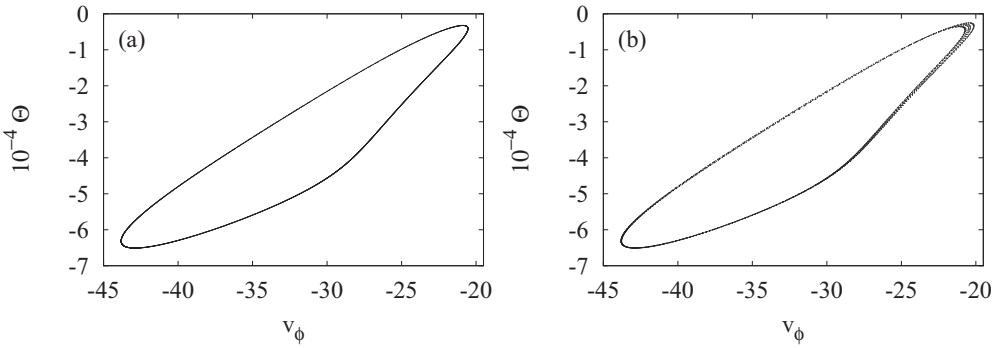

FIG. 5. Poincaré section at $\Theta((r_o+r_i)/2,0,3\pi/8)=0$ of the azimuthal component of the velocity field $v_\varphi(r_i+(r_o-r_i)/7,0,3\pi/8)$ plotted versus Θ at the same point. (a) Stable $m=1$ MRW at $\mathrm{Ra}=2.15701\times10^5$. (b) Stable three-tori bifurcated from the $m=1$ MRW at $\mathrm{Ra}=2.15685\times10^5$.

understood as trajectories that visit in a random way the stable RW and MRW, pointing out the interest of the computation of unstable solutions by continuation methods.

When the MRW lose their stability via Hopf bifurcations, branches of three-frequency solutions (three-tori) of Eq. (7) or two-frequency RW (two-tori) of Eq. (10) arise at the bifurcation points. By means of time integration of Eq. (7), the three stable three-tori bifurcated from the five- or sixfold MRW and the $m=1$ MRW have been found. The Poincaré section at $\Theta((r_o+r_i)/2,0,3\pi/8)=0$ of the azimuthal component of the velocity field $v_\varphi(r_i+(r_o-r_i)/7,0,3\pi/8)$ plotted versus Θ at the same point, for a stable $m=1$ MRW at $\mathrm{Ra}=2.15701\times10^5$, is displayed in Fig. 5(a). Figure 5(b) shows the same Poincaré section but for the stable three-tori at

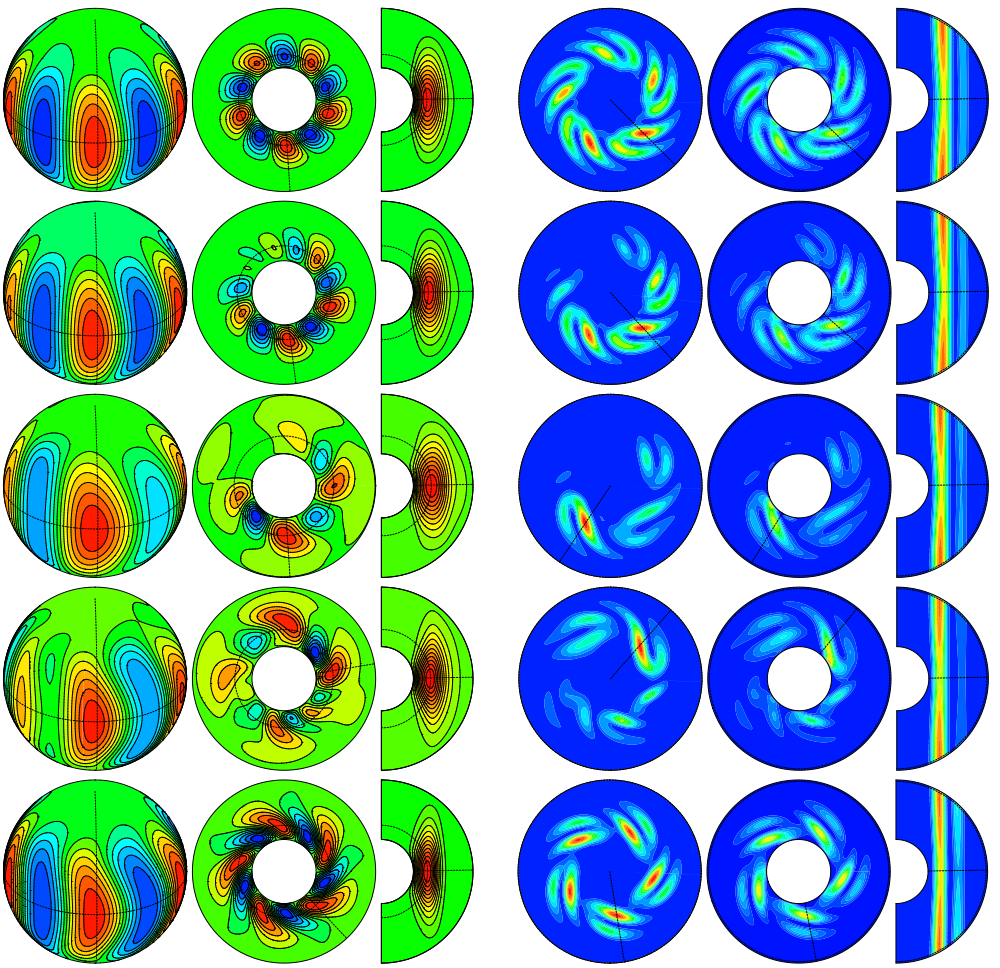

FIG. 6. The left column of three plots contains the contour plots of Θ on a sphere, on the equatorial plane, and on a meridional section, for solutions lying on the $m=1$ branch of MRW at $\mathrm{Ra}=2.04612\times10^5$, 2.20259×10^5, 3.23559×10^5, 4.31323×10^5, 4.87302×10^5 (from top to bottom). The right column corresponds to K for the solution and same Ra.

$\mathrm{Ra} = 2.15685 \times 10^5$, bifurcated from the $m = 1$ MRW. In this case the section is no longer a curve but a band. It is worth noticing that both types of oscillatory solutions are obtained from initial conditions given by the continuation code. Although they are stable near Ra_c, their stability interval is very short, and the basin of attraction of the stable five- or sixfold symmetric RW is much larger than that of the $m = 1$ MRW and three-tori of Eq. (7), then it would be almost impossible to get them by chance with time integrations.

The flow patterns along the $m = 1$ branch of MRW are shown in Fig. 6. It shows, from top to bottom, a sequence of solutions at $\mathrm{Ra} = 2.04612 \times 10^5$, 2.20259×10^5, 3.23559×10^5, 4.31323×10^5, 4.87302×10^5. Three projections of the temperature perturbation are displayed in the left group of plots. The radius of the spherical surfaces ranges from $r = r_i + 0.22d$ to $r = r_i + 0.3d$, although they are represented with the same size as the other sections. They correspond approximately to the location where the columns of Θ get the maximum. The middle projections are taken on the equatorial plane, and the right ones on a meridional section that cuts the equatorial cell of Θ by its maximum. The scale of colors is the same in each solution, with blue (dark gray) meaning cold fluid. The same projections are taken for the kinetic energy density K (right group of plots), but with the spherical projections taken close to the outer boundary at $r = r_i + 0.975d$, where it reaches its maximum at high latitudes, and with the spherical surface seen from the pole.

The meridional sections show the typical patterns of convection in a regime where rotation plays a dominant role in the dynamics: the z dependence of the flow is weak, and outside a columnar region the fluid is nearly stagnant. The cells of convection are symmetric with respect to the equatorial plane and attached to the inner sphere. The equatorial sections of K display a double-layered pattern of spiraling vortices. The solutions close to the fivefold RW have the symmetry weakly broken and the five convective cells have similar size (see first and last rows of Fig. 6). In contrast, far away the bifurcation points, the number of convective cells diminishes, some of them are significantly smaller than the others and the convection is localized in patches whose intensity grows and decays while the full pattern is rotating.

Contour plots along the fivefold branch of MRW at $\mathrm{Ra} = 2.73868 \times 10^5$, 3.32581×10^5, 4.00390×10^5, 5.22800×10^5, 5.82313×10^5 are shown in Fig. 7. The patterns of the first solution resemble those of the fivefold RW at the bifurcation point. As the Rayleigh number is increased,

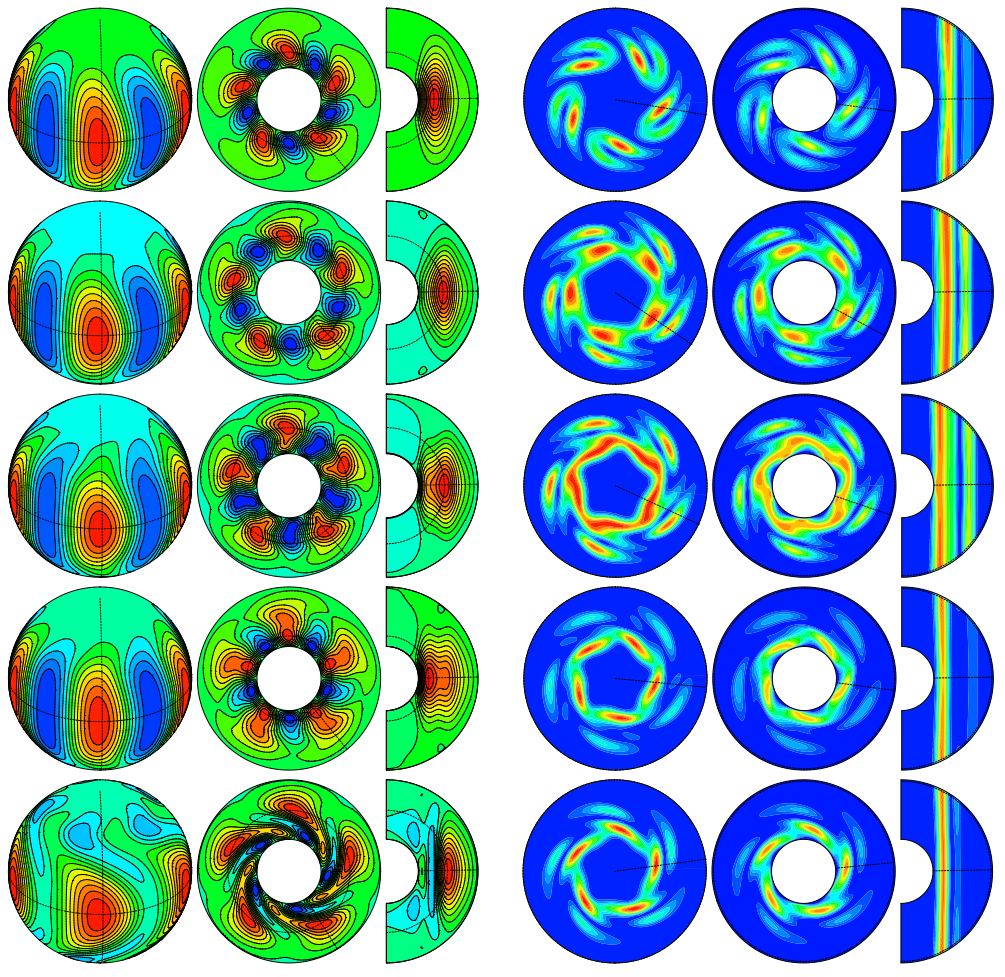

FIG. 7. Same contour plots as in Fig. 6 for fivefold symmetric solutions at $\mathrm{Ra} = 2.73868 \times 10^5$, 3.32581×10^5, 4.00390×10^5, 5.22800×10^5, 5.82313×10^5 (from top to bottom).

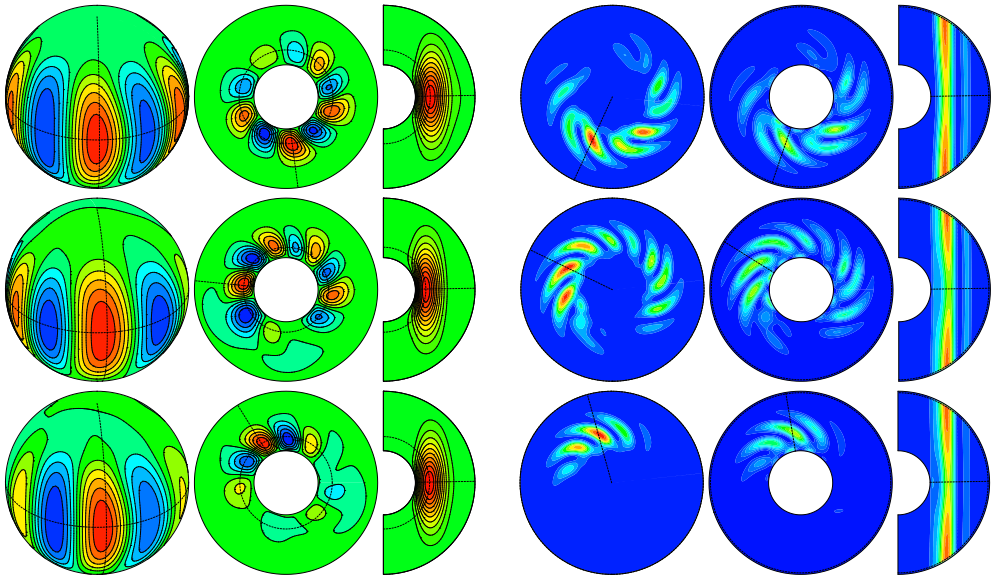

FIG. 8. Same type of contour plots as in Fig. 6. The first row corresponds to Θ and K for the solution at the first Hopf bifurcation point ($\mathrm{Ra}_2^1 = 2.15690 \times 10^5$) on the $m = 1$ branch, the next two rows show the real and imaginary parts of the leading eigenfunction at the same point.

the cells of hot fluid spiral and expand to the outer boundary, confining the cold fluid in small cells near the interior. In addition, the vortices of K become connected near the inner boundary, indicating that there are strong internal mean zonal circulations in this region of parameters (see for instance the third row at $\mathrm{Ra} = 4.00390 \times 10^5$). The same behavior was found when the sixfold MRW were analyzed.

Figures 8, 9, and 10 display, respectively, the contour plots of Θ and K for the $m = 1$ MRW, the five- or sixfold MRW at the Hopf bifurcation points where they lose stability, and the corresponding real and imaginary parts of the critical eigenfunction. At the bifurcation the symmetry of the five- or sixfold MRW is broken, but as can be seen in the second and third rows of Fig. 10 the eigenfunction of the sixfold MRW is invariant under a rotation of π. Therefore the three-frequency of waves emerging at this point retains a twofold rotational symmetry.

Finally, to check the sensibility of the bifurcation points with the spatial resolution, the variation of $\mathrm{Ra}, \tau, \omega$ and the argument of the leading eigenvalue, $\mathrm{Arg}(\lambda)$, is studied for the four bifurcations where the MRW become stable or unstable. The results are included in Table I. We have changed both the number of radial collocation points, n_r, and the spherical harmonics truncation parameter, $L_{\max}$. The computation of the five- or sixfold symmetric branches is performed applying symmetry constraints to reduce the size

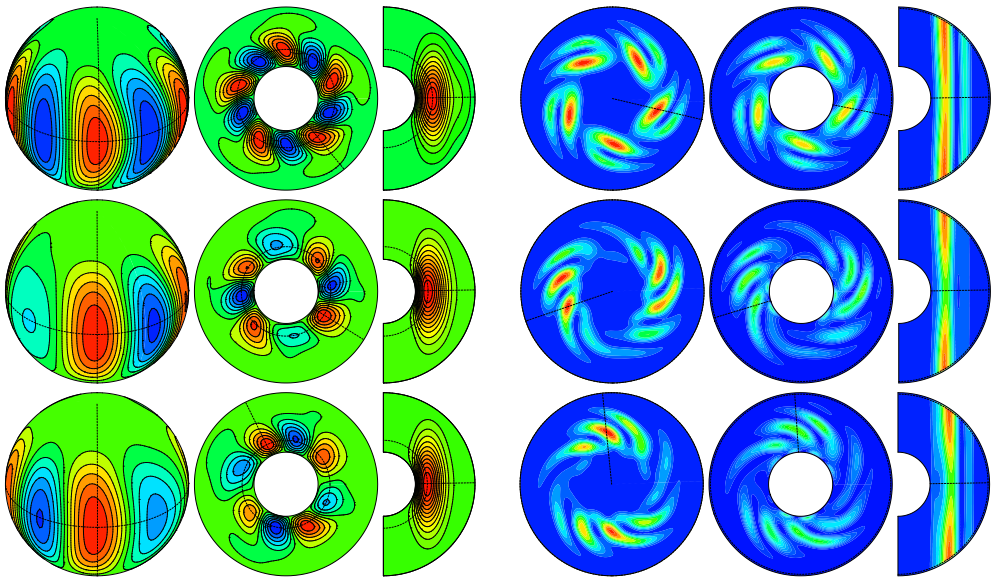

FIG. 9. Same contour plots as in Fig. 8 for the solution and the real and imaginary parts of the leading eigenfunction at the first Hopf bifurcation point ($\mathrm{Ra}_1^5 = 2.86197 \times 10^5$) on the fivefold branch.

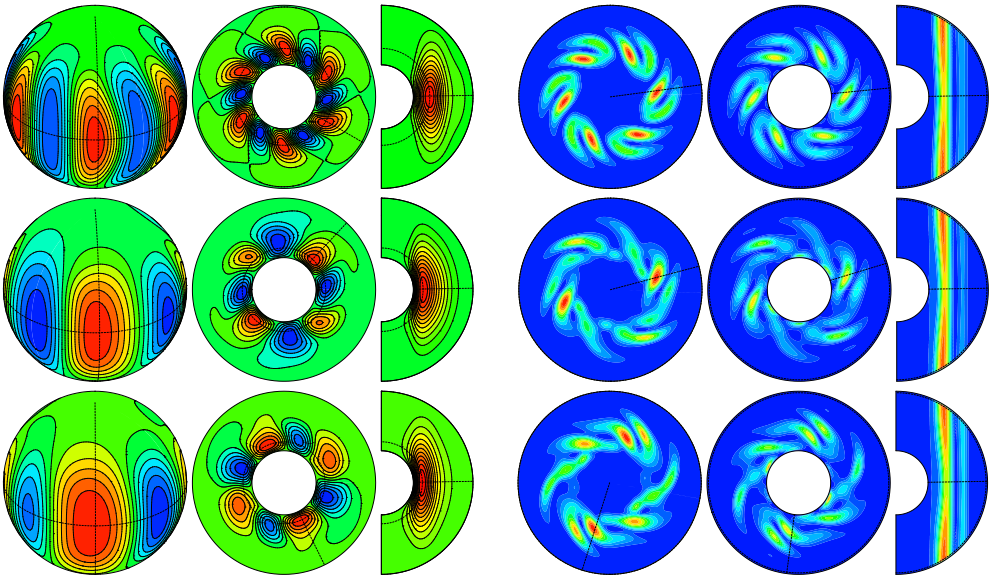

FIG. 10. Same contour plots as in Fig. 9 for the solution and the real and imaginary parts of the leading eigenfunction at the first Hopf bifurcation point ($\mathrm{Ra}_1^6 = 2.60701 \times 10^5$) on the sixfold branch.

of the systems, n, required to obtain them. In contrast, all the modes must be retained when computing the branch without rotational symmetry. The values of n range from 57 692 up to 1 061 977. When analyzing the stability of the solutions no symmetry constraints are imposed. In this case the number of discretization points range from 345 991 up to 1 061 977. The determination of the critical point was performed in each case by inverse interpolation.

As can be seen in the table the accuracy of the results is very good. Even with the lower resolutions used at least three significant figures are obtained for Arg(λ) and four or more for the other quantities.

VI. SUMMARY

Modulated thermal Rossby waves and their stability have been computed in rotating spherical geometry for parameter values of Pr and η of geophysical relevance.

The MRW have been obtained as periodic orbits in the rotating frame of reference where only the period of the modulation is observed. Newton-Krylov continuation allows us to obtain unstable RW and MRW that cannot be found by only using time integrations. The use of matrix-free linear solvers for the Newton iterations avoids the storage of the Jacobian matrix allowing us to tackle high resolutions needed for low Ekman and Prandtl number flows. In this way we have been able to compute stable MRW stabilized at a saddle-node bifurcation of an unstable branch of MRW.

To find a single MRW up to relative tolerance 10^{-8} the Newton-Krylov method typically converges in four Newton iterations. Each of them requires an evaluation of the function, i.e., one time integration of an ODE system of dimension $n = O(10^5 - 10^6)$ plus an average of 15 GMRES iterations, i.e., 15 additional time integrations of an ODE system of dimension $2n$ are needed. Close to the bifurcation points the convergence slows down, so efficient and accurate (high-order) time integration is essential.

TABLE I. Variation of the critical parameters of the MRW at the bifurcations where they change the stability with the resolution.

n_r	m	$\frac{L_{\max}}{m}$	n	Ra_c	τ	ω	Arg(λ)
32	1	60	345991	215713.2	0.0709448	90.6995	0
40	1	72	623415	215716.7	0.0709454	90.6989	0
50	1	84	1061977	215716.7	0.0709454	90.6989	0
32	1	60	345991	215689.7	0.0706949	90.7367	0.0388974
40	1	72	623415	215692.4	0.0706954	90.7363	0.0389272
50	1	84	1061977	215692.4	0.0706953	90.7363	0.0389286
32	5	12	69223	286197.3	0.0361569	80.7386	2.47680
40	5	14	117975	286203.6	0.0361561	80.7383	2.47700
50	5	16	192913	286203.8	0.0361561	80.7384	2.47701
32	6	10	57691	260700.8	0.0378892	63.2709	1.13710
40	6	12	103935	260703.5	0.0378885	63.2706	1.13703
50	6	14	177037	260703.4	0.0378885	63.2706	1.13704

We have performed an exhaustive stability analysis to detect and classify the large sequence of bifurcations that takes place along these branches. In contrast to what happens with the RW, we have found that the range of Ra in which the MRW are stable is very small. This is especially true in the case of the $m = 1$ MRW, stable very close to the onset at $\mathrm{Ra}/\mathrm{Ra}_c = 1.16$. The stability regions of the RW and MRW overlap giving rise to regions of multistability of two and three different types of waves.

The five- or sixfold and $m = 1$ MRW lose their stability via tertiary Hopf bifurcations, giving rise to three-frequency stable solutions. In addition, we have found more than 50 Hopf and period-doubling bifurcations along the branches of RW and MRW studied. These bifurcations give rise to branches of unstable modulated and three-frequency waves, which configure the skeleton of the phase space. To have the tools to compute them is important because the study of the unstable branches of solutions could explain the origin of stable temporally chaotic flows observed experimentally in the same range of parameters or computed from uncontrolled initial conditions.

ACKNOWLEDGMENTS

This research has been supported by MEC-DGICT/FEDER Project No. FIS2013-40674-P and AGAUR-GENCAT Project No. 2014-SGR-1145.

[1] M. R. E. Proctor and C. A. Jones, J. Fluid Mech. **188**, 301 (1988).
[2] C. A. Jones, A. M. Soward, and A. I. Mussa, J. Fluid Mech. **405**, 157 (2000).
[3] C. Egbers, W. Beyer, A. Bonhage, R. Hollerbach, and P. Beltrame, Adv. Space Res. **32**, 171 (2003).
[4] E.-J. Kim, D. W. Hughes, and A. M. Soward, Geophys. Astrophys. Fluid Dynam. **98**, 325 (2004).
[5] P. W. Livermore, D. W. Hughes, and S. M. Tobias, Phys. Fluids **19**, 057101 (2007).
[6] P. A. Davidson, Geophys. J. Inter. **195**, 67 (2013).
[7] C. A. Jones, Treat. Geophys. **8**, 131 (2007).
[8] P. Olson, Phys. Earth Planet. Inter. **187**, 1 (2011).
[9] D. Rand, Arch. Ration. Mech. An. **79**, 1 (1982).
[10] M. Golubitsky, V. G. LeBlanc, and I. Melbourne, J. Nonlin. Sci. **10**, 69 (2000).
[11] K. K. Zhang, Phys. Earth Planet. Inter. **72**, 236 (1992).
[12] M. Ardes, F. H. Busse, and J. Wicht, Phys. Earth Planet. Inter. **99**, 55 (1997).
[13] A. Tilgner and F. H. Busse, J. Fluid. Mech. **332**, 359 (1997).
[14] U. Christensen, J. Fluid Mech. **470**, 115 (2002).
[15] R. Simitev and F. H. Busse, New J. Phys. **5**, 97 (2003).
[16] F. Feudel, N. Seehafer, L. S. Tuckerman, and M. Gellert, Phys. Rev. E **87**, 023021 (2013).
[17] F. Garcia, J. Sánchez, E. Dormy, and M. Net, SIAM J. Appl. Dynam. Syst. **14**, 1787 (2015).
[18] G. Kawahara, M. Uhlmann, and L. van Veen, Ann. Rev. Fluid Mech. **44**, 203 (2012).
[19] H. B. Keller, in *Applications of Bifurcation Theory*, edited by P. H. Rabinowitz (Academic Press, New York, 1977), pp. 359–384.
[20] J. Sánchez, M. Net, B. García-Archilla, and C. Simó, J. Comput. Phys. **201**, 13 (2004).
[21] J. Sánchez and M. Net, Int. J. Bifurcat. Chaos **20**, 1 (2010).
[22] M. Net and J. Sánchez, SIAM J. Appl. Dynam. Syst. **14**, 674 (2015).
[23] T. Watanabe, K. Toyabe, M. Iima, and Y. Nishiura, in APS Division of Fluid Dynamics Meeting Abstracts (2010), p. H7.
[24] H. A. Dijkstra, F. W. Wubs, A. K. Cliffe, E. Doedel, I. F. Dragomirescu, B. Eckhardt, A. Gelfat, A. Hazel, V. Lucarini, A. Salinger, J. Sánchez, H. Schuttelaars, L. Tuckerman, and U. Thiele, Commun. Comput. Phys. **15**, 1 (2014).
[25] I. C. Waugh, S. J. Illingworth, and M. P. Juniper, J. Comput. Phys. **240**, 225 (2013).
[26] I. C. Waugh, K. Kashinath, and M. P. Juniper, J. Fluid Mech. **759**, 1 (2014).
[27] D. Viswanath, J. Fluid Mech. **580**, 339 (2007).
[28] J. Sánchez, M. Net, and C. Simó, Physica D **239**, 123 (2010).
[29] J. Sánchez and M. Net, Physica D **252**, 22 (2013).
[30] L. van Veen, G. Kawahara, and M. Atsushi, SIAM J. Sci. Comput. **33**, 25 (2011).
[31] K. Kimura, S. Takehiro, and M. Yamada, Phys. Fluids **23**, 074101 (2011).
[32] J. Sánchez, F. Garcia, and M. Net, Phys. Rev. E **87**, 033014 (2013).
[33] F. Garcia, M. Net, B. García-Archilla, and J. Sánchez, J. Comput. Phys. **229**, 7997 (2010).
[34] F. Garcia, E. Dormy, J. Sánchez, and M. Net, in Proceedings of the 5th International Conference on Computational Methods—ICCM2014. Cambridge, England, edited by G. R. Liu and Z. W. G. (ScienTech Publisher, 2014), vol. 1.
[35] M. Frigo and S. G. Johnson, Proceedings of the IEEE **93**, 216 (2005), special issue on Program Generation, Optimization, and Platform Adaptation
[36] K. Goto and R. A. van de Geijn, ACM Trans. Math. Softw. **34**, 1 (2008).
[37] F. Garcia, J. Sánchez, and M. Net, Phys. Rev. Lett. **101**, 194501 (2008).
[38] R. B. Lehoucq, D. C. Sorensen, and C. Yang, *ARPACK User's Guide: Solution of Large-Scale Eigenvalue Problems with Implicitly Restarted Arnoldi Methods* (SIAM, Philadelphia, 1998).
[39] K. Meerbergen and D. Roose, IMA J. Num. Anal. **16**, 297 (1996).
[40] Y. Saad and M. H. Schultz, SIAM J. Sci. Stat. Comput. **7**, 856 (1986).
[41] F. Garcia, Ph.D. Thesis, Universitat Politècnica de Catalunya (2012).
[42] F. Garcia, J. Sánchez, and M. Net, Phys. Earth Planet. Inter. **230**, 28 (2014).
[43] A. Palacios, Discrete Cont. Dynam. B **2**, 129 (2002).